# Aperiodic incommensurate phase of a $C_{60}$ monolayer on Ag(100)

Ching-Ling Hsu and Woei Wu Pai*

*Center for Condensed Matter Sciences, National Taiwan University, Taipei, Taiwan, Republic of China*
(Received 30 June 2003; published 15 December 2003)

Detailed combined scanning tunneling microscopy and low-energy electron diffraction measurements reveal that the structure of a $C_{60}$ monolayer on Ag(100) is not the previously accepted commensurate $c(6\times4)$ phase but rather an incommensurate (111) close-packed phase. The film exhibits a characteristic molecular contrast pattern with merely short-range order, and room-temperature fluctuations of the contrast show that a thermal equilibrium state is reached. The nature of this controversial bright-dim $C_{60}$ contrast is clarified as a topographic feature due to $C_{60}$-induced reconstruction underneath the dim $C_{60}$ molecules. Due to interactions between the incommensurate $C_{60}$ adlayer and the reconstructed substrate, the (111) phase is distorted laterally, forming a novel "tetramer" configuration of specific contrast order. The spatial distribution of these tetramers is aperiodic; this has crucial implications for the peculiar short-range contrast order observed experimentally. A lattice gas model with anisotropic nearest-neighbor interactions and a configuration energy of the tetramer is developed. Quantitative agreements between observation and modeling are achieved with reasonable phenomenological parameters derived within experimental constraints.

## I. INTRODUCTION

Recently, many studies have focused on the adsorption and growth of $C_{60}$ on various surfaces. For $C_{60}$ adlayers grown on metal surfaces, understanding the structures and the interactions between $C_{60}$ and the substrates has attracted much research effort.[1–3] It is known that molecular orbitals of $C_{60}$ hybridize with the substrates, leading to various bonding characteristics[4] and different degrees of charge transfer. Meanwhile, the intermolecular van der Waals interaction retains its important role. In spite of substrate symmetry, $C_{60}$ adlayers still prefer nearly close-packed hexagonal or quasi-hexagonal packings, and the nearest-neighbor (NN) $C_{60}$-$C_{60}$ distances show slight variations in adjustment to strain. Consequently, their structures are generally determined by these competing adsorbate-adosorbate and adsorbate-substrate interactions, as well as influence of molecular packing due to $C_{60}$-induced substrate reconstruction.[5–7] $C_{60}$ adlayers grown on metal surfaces also display rich electronic phenomena; $C_{60}$-based fullerides are considered model systems to explore key conceptual issues in strongly correlated physics,[8] and their possible use in molecular electronics is also actively explored.

Given their fundamental and practical relevance, the structures and properties of $C_{60}$-based films are still actively studied regardless of intense research efforts during the past decade.[1,3] In this study, we have chosen a system, i.e., a monolayer $C_{60}$ on Ag(100), that has unusual aspects. First, these $C_{60}$ exhibit a distinct $\sim 1-2$ Å bright and dim scanning tunneling microscopy (STM) contrast arranged with intricate short-range order, even after sufficient annealing. Second, the charge transfer from Ag to $C_{60}$ is so strong ($\sim 2-3$ $e^-$ per $C_{60}$) that the bonding is characterized as predominantly ionic.[9] Finally, a temperature-dependent and reversible gap opening at the Fermi energy has recently been reported,[10] implicating a surface superconductivity. A similar gap-opening transition is not observed for $C_{60}$ on other Ag faces, e.g., (110).[10] This indicates a specificity of the structure-property relationship in this film structure. So far, the contrast mechanism remains under debate, and the physical origins of the peculiar ordering and the gap-opening transition are basically unknown. These peculiar and unresolved issues make $C_{60}$/Ag(100) unique among the many studied $C_{60}$/metal systems, hence the importance in understanding the factors underlying these unique behaviors.

Here we report a comprehensive study of the $C_{60}$/Ag(100) film structure using STM and low-energy electron diffraction (LEED). We clarify the nature of the bright-dim contrast and categorize basic ordering patterns. A major revision on the adsorption structure is reported; the $C_{60}$ film forms an incommensurate (111) close-packed hexagonal phase, instead of the previously accepted commensurate $c(6\times4)$ phase.[10–12] We have also characterized in detail the in-plane distortion of this $C_{60}$ film. It shows that there is a random spatial distribution of a novel distorted configuration that renders the film aperiodic. The observed incommensurability is surprising as the adsorbate-substrate interaction is believed to be strong in this system. Finally, we develop a lattice gas model to shed light on the competing interactions underpinning the observed contrast ordering.

## II. EXPERIMENT

Sample preparation and measurements proceeded in a homebuilt ultrahigh-vacuum chamber (base pressure $\sim 4 \times 10^{-11}$ torr) housing standard surface analytical tools (Auger, LEED) and a commercial variable-temperature multi-mode scanning probe microscope (Omicron VT-SPM). Both STM and beam-deflected-type noncontact[13] atomic force microscopy (AFM) measurements can be conducted with the microscope. A spot-profile analysis low-energy electron diffractometer (SPA-LEED) and a conventional LEED apparatus, with transfer widths of $\sim 1200$ Å and $\sim 300$ Å, respectively, were used to record LEED patterns. Results obtained were basically identical except the SPA-LEED achieved superior momentum resolution ($<0.01$ Å$^{-1}$).

The Ag(100) surface was cleaned by repeated cycles of neon sputtering and annealing ($\sim 800$ K), and its contamination level was checked by Auger spectroscopy and directly with STM. $C_{60}$ ($>99.95\%$ purity) was deposited from an electron-beam evaporator with a thoroughly outgased Ta crucible. The pressure was kept under $<10^{-10}$ torr during deposition. Typical substrate temperature during the $C_{60}$ deposition was $\sim 460$ K and the nominal deposition rate $\sim 0.05-0.2$ ML/min (1 ML (monolayer) = fully covered $C_{60}$). Several different deposition conditions were also used, including multilayer growth at room temperature with subsequent desorption at $>500$ K and direct deposition of $C_{60}$ film onto the Ag(100) held at $\sim 700$ K.[10] Results obtained were identical and no obvious effect of deposition temperature on the $C_{60}$ ordering was observed. For the preparation of an ordered $C_{60}$ film without the $C_{60}$-induced reconstruction, a lower substrate temperature 250–260 K and a lower deposition rate were used. The sample temperature on the sample-mounted manipulator head was monitored by a calibrated thermocouple, and the temperature on the STM stage was measured by a Si diode mounted on a cooling block in direct thermal contact with the Ag crystal. The STM observations proceeded in the temperature range from 100 to 350 K, and the LEED measurements were conducted at room temperature.

## III. RESULTS AND DISCUSSION

### A. General STM features of a monolayer $C_{60}$ on Ag(100)

$C_{60}$ monolayers on Ag(100) have been studied with STM and scanning tunneling spectroscopy (STS) by several groups.[9–12,14–18] Several structural characteristics have been identified, which are summarized below. As previously noted, a single-layer $C_{60}$ film aggregates mainly at step edges. Two coexistent orthogonal domains are also seen, reflecting the symmetry of an fcc (100) substrate. A distinct molecular contrast appears in an annealed $C_{60}$ film. The contrast height between the bright- (**B**-) and dim- (**D**-) type $C_{60}$ molecules is approximately $1\sim 2$ Å,[12,17] as shown in Figs. 1(a) and 1(b). The contrast height varies slightly depending on tunneling conditions. However, it rarely exceeds 2 Å. Therefore, the bright and dim $C_{60}$ clearly belong to the same monolayer. A second layer $C_{60}$ grown on top of the first looks much flatter.[15] In addition to the **B**- and **D**-type $C_{60}$, a previously unreported medium (**M**) species is also found, as shown in Fig. 1, inset. The emergence of the bright-dim contrast is a thermally activated and irreversible process.[15,17] Upon annealing, the dim $C_{60}$ emerge at $\sim 280$ K while the remaining bright $C_{60}$ are unchanged.[15]

In addition to the characteristic **B**-**D** contrast, the $C_{60}$ film exhibits rather complicated contrast patterns. The contrast seems to possess merely short-range order, instead of any long-range order. Several basic contrast patterns can be categorized: see Sec. III D. In a particular domain, the contrast pattern exhibits anisotropy, with (discontinuous) zigzag rows orienting in one of the two close-packed [110] substrate directions. This pattern is unique among the fullerene/metal systems exhibiting **B**-**D** $C_{60}$ contrasts. The latter include $C_{60}$
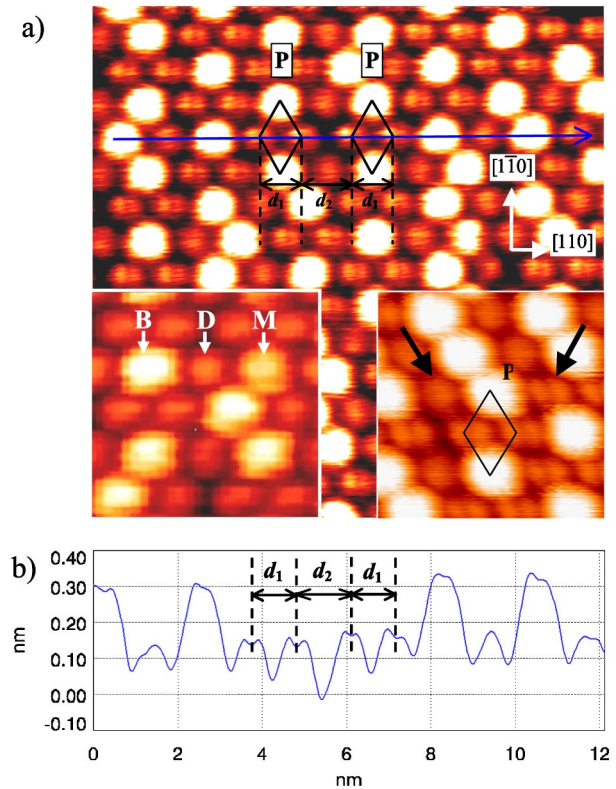


FIG. 1. (Color online) (a) A room-temperature $C_{60}$/Ag(100) STM image with the bright and dim $C_{60}$ contrast. Lower left inset shows the presence of the bright (**B**), dim (**D**), and medium (**M**) contrast $C_{60}$ species. The rhombic parallelogram **P** is a configuration with specific contrast arrangement in which two dim $C_{60}$ are paired along [110] and sandwiched by two bright $C_{60}$ aligned along [1$\bar{1}$0]. All dim $C_{60}$ in the **P** configuration show an intramolecular nodal feature whereas the other dim $C_{60}$ appear round and featureless (lower right inset). Image size $12 \times 14$ nm$^2$, sample bias $-1.0$ V, and tunneling current 0.8 nA. (b) The profile of $C_{60}$ molecules along [110] reveals that the nearest-neighbor distance between two dim $C_{60}$ varies due to the pairing phenomenon. The shortened $C_{60}$-$C_{60}$ distance $d_1 = (9.5 \pm 0.2)$ Å and the lengthened $d_2 = (11.1 \pm 0.2)$ Å.

on Ni(110),[19] Au(110),[6] Pd(110),[7,20] and Al(111),[4] where the well-annealed films show long-range contrast order. On the other hand, the short-range contrast order of $C_{60}$/Ag(100) is not simply associated with metastable states, but persists after extensive annealing and therefore cannot easily be reconciled with surface reconstructions in $C_{60}$/Ag(100). Offered explanations include different $C_{60}$ bonding orientations,[16] rotational order and disorder,[14] and the onset of charge transfer[17] but confusions remain.

Nevertheless, a converging consensus is that the contrast is indeed a topographic feature involving substrate reconstruction. The evidence comes from several perspectives. For example, a low-temperature STM and STS study[18] shows that local spectroscopic characteristics are insensitive to $C_{60}$ molecular orientations and **B**-**D** types. Pai et al.[15] have examined the temperature evolution of the $C_{60}$ contrast and found that the bright $C_{60}$ turns into the dim $C_{60}$ above $\sim 280$ K. Based on simulated contrast evolution of a

multilayer C$_{60}$ film as well as molecular-resolved noncontact AFM measurements, Pai *et al.* argued for a topographic nature of the **B**-**D** contrast. These findings conform to the general idea that C$_{60}$ molecules form chemical bonds with metal surfaces and in turn alter the underlying substrate atomic arrangement to increase the C$_{60}$-metal coordination, with a sufficient energy gain to overcome substrate reconstruction. These higher-coordinated C$_{60}$ will appear lower in height in STM images.

In addition to the topographic vertical corrugation in the C$_{60}$ film, we report here new observations of significant lateral adlayer distortion. The latter phenomenon is due to an incommensurability between the C$_{60}$ layer and the reconstructed substrate, and furthermore eliminates long-range order in C$_{60}$/Ag(100), to be discussed in the next section. In Fig. 1(b), the depicted profile of several dim C$_{60}$ molecules in series along [110] clearly indicates that some C$_{60}$ have arranged in pairs. The shortened C$_{60}$-C$_{60}$ distance $d_1$ is $(9.5\pm0.2)$ Å and the lengthened $d_2$ is $(11.1\pm0.2)$ Å. Closer inspection reveals that such C$_{60}$ pairs always necessitate a novel local configuration; it consists of two dim C$_{60}$ paired along [110] and sandwiched by two bright C$_{60}$ aligned along [1$\bar{1}$0], forming a rhombic tetramer as shown by **P** in Fig. 1(a). Only the dim molecules participating in this unique configuration are displaced laterally. This configuration, not previously reported, plays an important role in stabilizing the peculiar contrast pattern, as we shall argue in Sec. III F. We also point out that the distribution of the tetramers is random. The C$_{60}$ film is therefore *aperiodic*, without translational invariance. This may have a significant influence on the electronic properties of the C$_{60}$ film. Lattice aperiodicity often leads to a "pseudogap" with a reduced density of states at the Fermi energy, because the reciprocal space is populated with numerous Bragg planes instead of a single well-defined Bragg plane.[21] It is therefore possible that the electronic gap opening found in Refs. 10 and 11 relates to this adlayer aperiodicity rather than the onset of superconductivity. In particular, in Ref. 10 the authors have suggested that the expanded C$_{60}$-C$_{60}$ lattice constant (i.e., 10.54 Å) in the $c(6\times4)$ phase could help the development of surface superconductivity. As we will show in the next section, the NN C$_{60}$-C$_{60}$ distance, 10.0 Å, is actually the same as that in a bulk C$_{60}$ crystal. It is fair to say that the correlation between the geometrical and electronic properties of this system remains unresolved.

### B. Incommensurability of C$_{60}$ on Ag(100)

Previous studies have assigned the $c(6\times4)$ adsorption structure for the monolayer C$_{60}$ on Ag(100). This assignment requires revision as we shall now discuss. In Fig. 2, the LEED pattern is consistent with two coexistent orthogonal domains of a close-packed (111) C$_{60}$, but inconsistent with the previously accepted $c(6\times4)$ structure. Indeed, all angles between adjacent (01) spots are measured to be 60° ($\pm1°$) instead of the expected 67.4° or 56.3° in the latter. The lattice constant of the C$_{60}$ layer is calculated from the magnitude of (01) beam vectors to be $(10.0\pm0.3)$ Å, the same as the NN distance of two C$_{60}$ in bulk C$_{60}$.[22] This indicates that
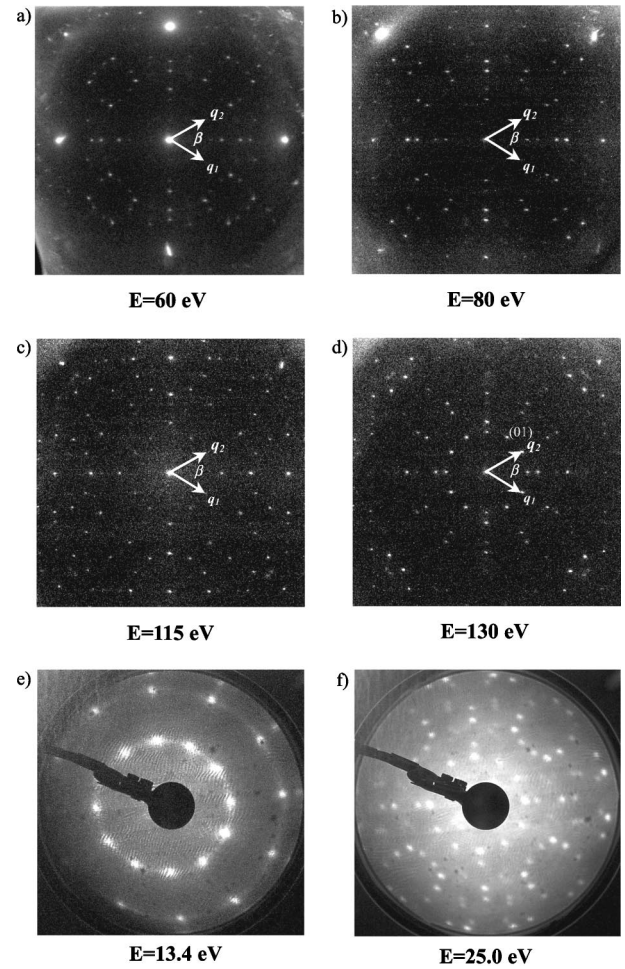


FIG. 2. (a)–(d) show four SPA-LEED patterns taken at beam energies 60, 80, 115, and 130 eV, respectively. The two unit vectors $q_1$ and $q_2$ form an angle $\beta\sim60°$ ($\pm1°$) and satisfy $|q_1|=|q_2|\sim(0.72\pm0.02)$ Å$^{-1}$. The LEED patterns are consistent with two coexistent 90° orthogonal domains of a close-packed (111) C$_{60}$ with a lattice constant of $\sim10.0$ Å. Additional multiple-scattering spots are also observed [see Fig. 4(c)]. (e) A LEED pattern of $\sim5$ ML C$_{60}$ grown on Ag(100) at room temperature. Beam energy$=13.4$ eV. Note the absence of the multiple-scattering spots due to the substrate. (f) A LEED pattern of the monolayer C$_{60}$ after subsequent desorption of the 5 ML C$_{60}$ film at $>500$ K for several minutes. Beam energy$=25.0$ eV.

the van der Waals interaction is crucial in determining the adsorption structure. This may appear surprising at first glance because studies have shown C$_{60}$ chemisorbs on Ag(100) with a significant charge transfer $\sim2-3\,e^-$ per C$_{60}$,[9,16] implying strong adsorbate-substrate interactions. In fact, an incidental lattice coincidence is the underpinning cause for the incommensurate phase. If one compares the adsorption sites in the $c(6\times4)$ and (111) phases, one finds that the NN distances along [1$\bar{1}$0] (defined as the direction perpendicular to both the close-packed directions of the substrate and the adlayer; see Fig. 1) are almost identical, as $6a_{Ag}$ ($a_{Ag}=2.89$ Å)$\approx17.33$ Å$\approx\sqrt{3}d$ ($d=10.0$ Å). In the [110] direction orthogonal to [1$\bar{1}$0], however, the average 10-Å C$_{60}$-C$_{60}$ separation is close to $2\sqrt{3}a_{Ag}\approx7/2a_{Ag}$. There-

fore, while the observed (111) phase is incommensurate, it almost matches a higher-order commensurate phase with a $(6 \times 7)$ unit cell containing four $C_{60}$. This allows the (111) phase to optimize its van der Waals interactions without a severe penalty in energy when a full commensurability is lost. Indeed, we shall argue that a portion of $C_{60}$ may sit in $(6 \times 7)$ unit cells while the rest are packed in a way to compensate strain. We shall return to this point in Sec. III D as we discuss one of the basic $C_{60}$ contrast patterns (i.e., "honeycomb" pattern) in the $C_{60}$ adlayer. The LEED pattern does reflect the average lattice periodicity because the lateral distortions of the ideal (111) phase do not have spatial long-range order.

We have also confirmed the (111) incommensurate phase with calibrated STM measurements. Note that the $c(6 \times 4)$ phase and (111) phase have nearly identical $C_{60}$-$C_{60}$ distances along $[1\bar{1}0]$ and there are two orthogonal $C_{60}$ domains. One can then use the $[1\bar{1}0]$ NN distance in one domain as a "ruler" to measure the (unknown) $[110]$ NN distance in the other. This procedure requires taking a STM micrograph containing a domain boundary. An example is shown in Fig. 3. Here the $C_{60}$-$C_{60}$ distance in the **A** domain along $[1\bar{1}0]$ is taken as 17.32 Å. Using this value as a calibrated ruler we find that the NN distance along $[110]$ in the **B** domain is 10.01 Å, in complete accordance with the LEED measurements.

One might ponder why the previous experiments[10,12,14,17] have not identified the (111) adlayer symmetry correctly. A possible source of confusion is the many additional spots due to strong multiple scattering in LEED. These additional spot positions are those (111) spots shifted by the reciprocal lattice vectors of Ag(100). An immediate consequence of the multiple scattering is the presence of repeated spots surrounding all substrate diffraction peaks. This can mistakenly implicate a commensurate adlayer. Here we give a full account of the LEED patterns observed at different beam energies. The collection of all LEED spots allows direct comparisons with the simulated LEED patterns of the $c(6 \times 4)$ phase and the close-packed (111) $C_{60}$ phase. Figures 2(a)–2(d) show four SPA-LEED patterns taken at 60, 80, 115, and 130 eV. A composite pattern with all spots from Figs. 2(a)–2(d) is consistent with Fig. 4(c). This is to be compared with Fig. 4(a), the $c(6 \times 4)$ LEED pattern, Fig. 4(b), the (111) close-packed phase without multiple scattering, and Fig. 4(c), the (111) close-packed phase with multiple-scattering spots. In pattern (c) the original (111) spots are denoted by solid dots and the multiple-scattering spots are denoted by circles. Clearly, the full match between the composite pattern and the simulated pattern (c) justifies our LEED assignment. We note that different deposition temperatures ($>460$ K) and procedures result in identical $C_{60}$ ordering. Figures 2(e) and 2(f) are the LEED patterns of a multilayer ($\sim 5$ ML) $C_{60}$ film and the monolayer $C_{60}$ film after subsequent desorption at $>500$ K,[10] respectively. The LEED pattern of Fig. 2(f) also conforms completely with Fig. 4(c).

Note that all observed LEED spot positions along $[1\bar{1}0]$ remain unchanged from that of the $c(6 \times 4)$ phase. As discussed earlier, the lattice incommensurability can be re-
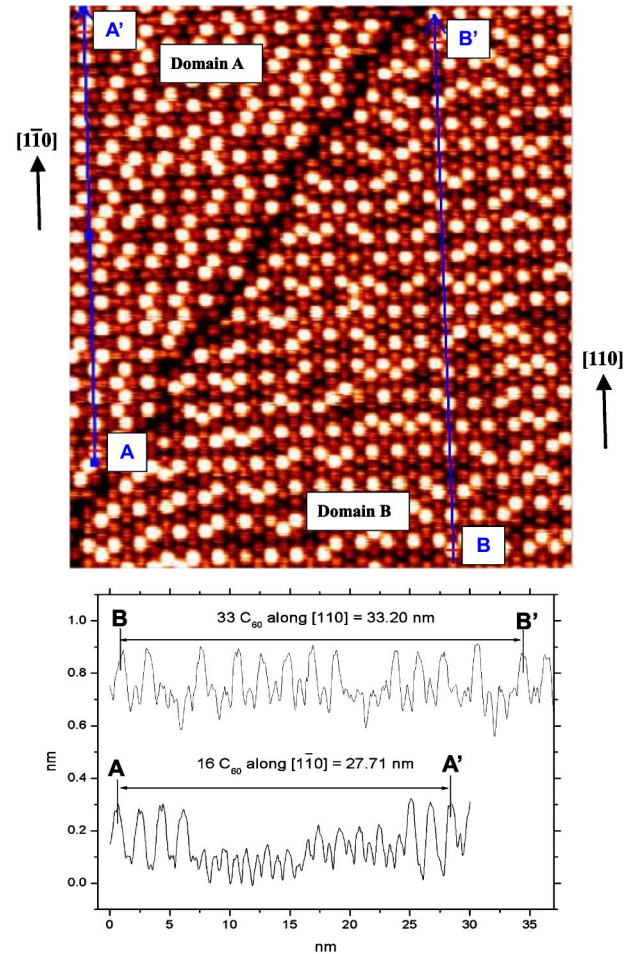


FIG. 3. (Color online) An STM image of a two-domain boundary for calibrating the NN $C_{60}$-$C_{60}$ distance. Using the $C_{60}$-$C_{60}$ distance 17.32 Å in the **A** domain along $[1\bar{1}0]$ as a calibrated ruler (16 $C_{60}$-$C_{60}$ spacing along $[1\bar{1}0]=27.71$ nm), the NN distance along $[110]$ in the **B** domain is determined to be $\sim 10.01$ Å (33 $C_{60}$-$C_{60}$ spacing along $[110]=33.20$ nm). This agrees completely with the LEED measurements. Image size $29 \times 33$ nm$^2$, sample bias $-1.7$ V, and tunneling current 0.8 nA.

garded as occurring purely in the $[110]$ direction. A schematic diagram of an overlapped close-packed (111) $C_{60}$ layer and the Ag(100) lattice is shown in Fig. 5(a) in which a best possible commensurability between the $C_{60}$ adlayer and Ag(100) substrate is assumed. That is, the NN $C_{60}$ spacing along $[110]$ is taken as $7/2a_{Ag}$ for simplicity. In this way, the registry of $C_{60}$ on the substrate along $[110]$ becomes alternate. If a $C_{60}$ sits at the bridge site midway between adjacent Ag atoms, the next $C_{60}$ in the $[110]$ direction would be on a hollow site [e.g., row **A** in Fig. 5(a)]. A row of $C_{60}$ (row **B**) subsequently stacked on the row **A** will adsorb on non-high-symmetry sites midway between the hollow and bridge sites. This unfavorable situation may be remedied by displacing $C_{60}$ toward preferred binding sites (e.g., hollow sites). The physics of such a process is similar to the well-known Frenkel-Kontorova (FK) model.[23] In this paper we will not pursue a quantitative FK model analysis. We simply point out that the $C_{60}$-induced substrate reconstruction should pre-
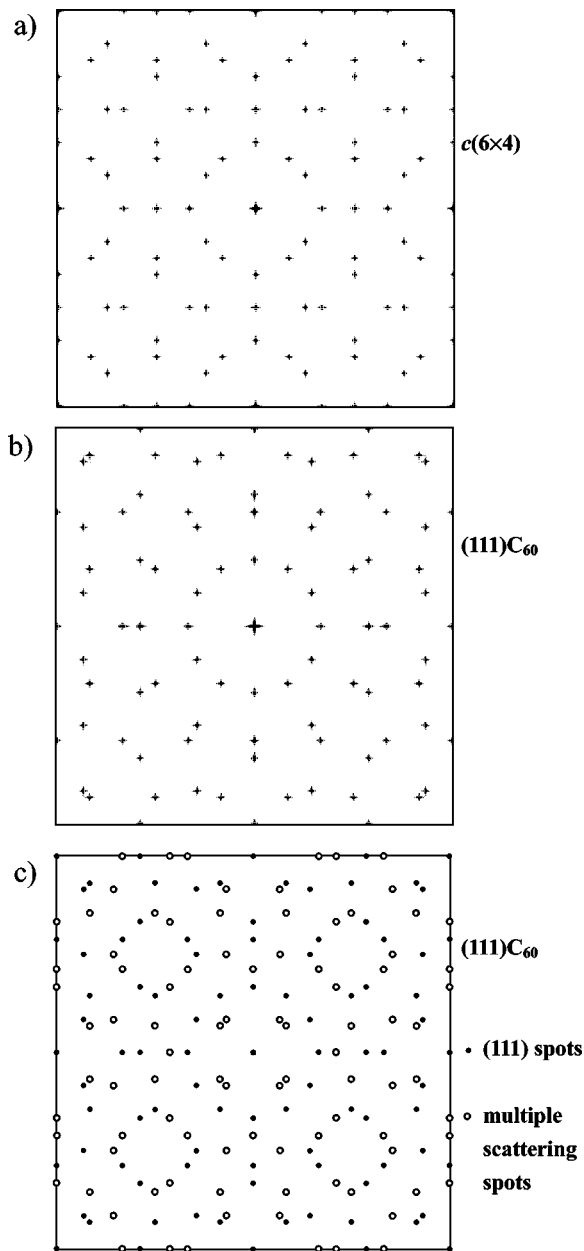
FIG. 4. LEED schematics: (a) the $c(6\times4)$ LEED pattern, (b) the (111) close-packed phase without multiple scattering, and (c) the (111) close- packed phase with multiple-scattering spots shifted by the reciprocal lattice vectors of Ag(100). The original (111) spots are denoted by solid dots and the multiple-scattering spots are denoted by circles. The pattern (c) is completely consistent with our LEED assignment shown in Fig. 2.



FIG. 5. (Color online) (a) A schematic diagram of an overlapped close-packed (111) C$_{60}$ layer and the Ag(100) lattice. Approximating the NN C$_{60}$ spacing along [110] by $3.5a_{Ag}$ ($10.0$ Å$\approx3.46a_{Ag}$), the registry of row **A** C$_{60}$ on the substrate along [110] becomes alternate bridge and hollow sites. The subsequently stacked row **B** C$_{60}$ adsorb on non-high-symmetry sites midway between the hollow and bridge sites. (b)–(e) show the schematics of lattice displacements of all four basic contrast patterns. Each arrow indicates a shift of the C$_{60}$ position by $1/4a_{Ag}$. Each arrow with a "$\times2$" mark denotes a shift of the C$_{60}$ position by $2/4a_{Ag}$.

### C. Substrate mass transport and a "pit" reconstruction model

In Sec. III A, we have reviewed the basic STM findings for a monolayer C$_{60}$ on Ag(100). The bright-dim contrast, often considered as a straightforward signature of a height variation, is used to infer adsorbate-induced reconstruction in several fullerene films grown on metal surfaces.[4,6,7,19,20] The contrast of C$_{60}$ on Ag(100), however, remains ambiguous, partly due to the intricate ordering with merely short-range order even at thermal equilibrium. Our previous study reveals that all low-temperature deposited C$_{60}$ are "bright," but can evolve into the "dim" type upon annealing.[15] This evidence led us to reconsider local surface reconstruction as the origin of the **B-D** contrast. Any electronic origin is also rejected by STS performed at 4 K.[18] This work affirms no significant difference in the C$_{60}$-Ag bonding character between different molecule types.

It is necessary to draw a definite conclusion on the nature of the **B-D** contrast as a prerequisite to understand its ordering. To further understand the possible coordination and

fer to occur at a specific adsorption site, because different adsorption energy gains are involved. This is mostly pertaining to an incommensurate phase, as we have observed here, or a higher-order commensurate phase due to multiplicity of adsorption sites. From the above argument we provide a basis on how the adlayer incommensurability may affect the state of interfacial reconstruction. This in turn has implications for the formation and distribution of the bright-dim STM patterns, to be further discussed in Secs. III D and III E.
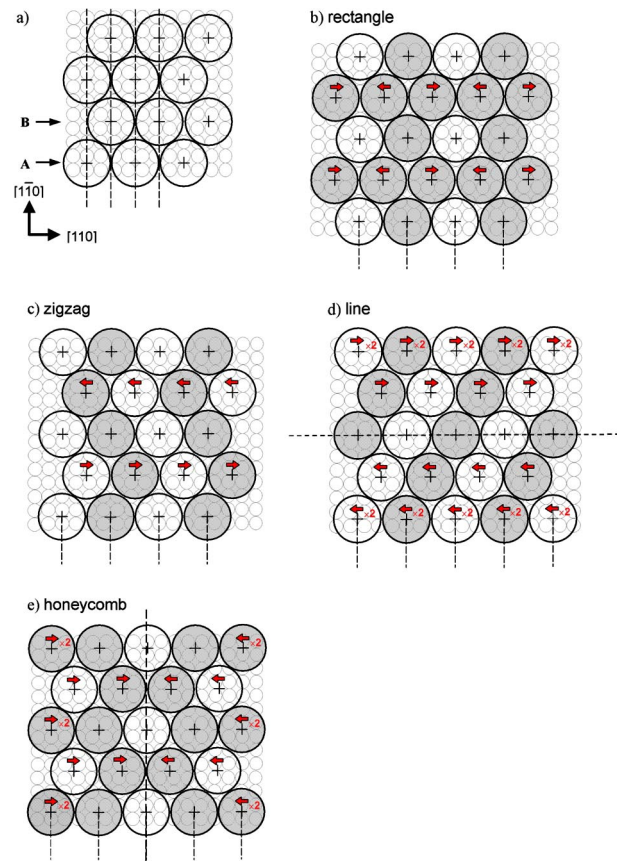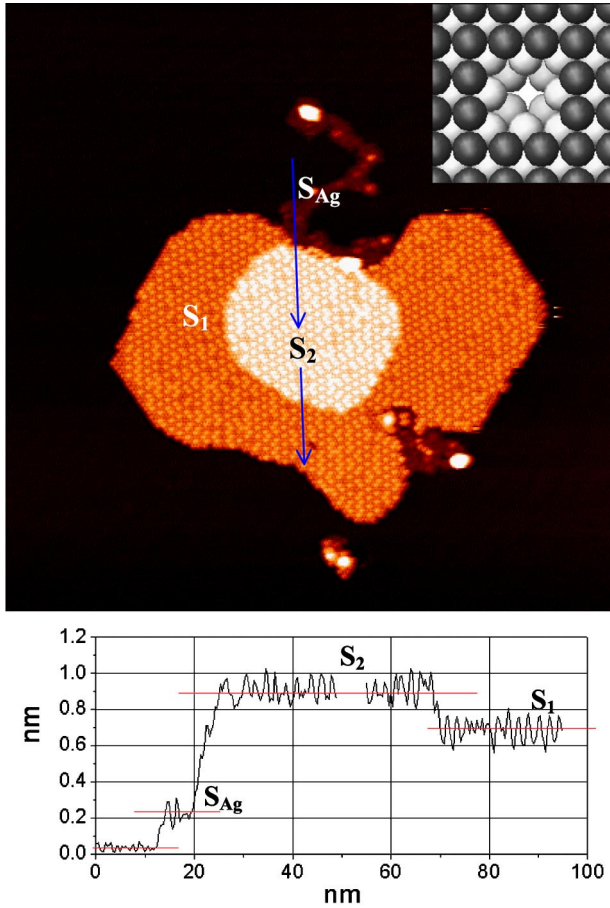
FIG. 6. (Color online) A double-layer $C_{60}$ island prepared at $\sim 350$ K. The Ag atoms displaced by the dim $C_{60}$ nucleate underneath the original $C_{60}$ layer and raise the $C_{60}$ layer by $\sim 2$ Å. $S_1$, $S_2$, and $S_{Ag}$ denote the areas for the original $C_{60}$ region, the "raised" $C_{60}$ region, and the extra bare silver region, respectively. Image size $150 \times 150$ nm$^2$, sample bias $-1.0$ V, and tunneling current 0.8 nA. The inset shows the schematics of a plausible restructuring model underneath each dim $C_{60}$ (see text).

structure of the reconstructed interface, we examine in detail silver substrate mass transport in the formation of a contrasted $C_{60}$ layer. This will not only reveal long-range mass transport accompanying the "dim"-type $C_{60}$, but will also shed new light on plausible structures of the reconstructed interface underneath these "dim" $C_{60}$.

Observation of mass flow requires specific film growth conditions. Above 380 K, $C_{60}$ on Ag(100) are highly mobile and they nucleate preferentially at steps, showing few, if any, evidence of substrate mass transport. When the deposition temperature is lower than 270 K, no **B-D** contrast, i.e., surface reconstruction, appears. If we prepare the $C_{60}$ film at around 350 K ($\pm 10$ K), significant displacement of silver atoms is observed; new Ag islands may nucleate, especially on wide terraces. Such islands can rest below the original $C_{60}$ adlayer, forming a peculiar double-layer $C_{60}$ island structure. Figure 6 gives an example. There, the raised $C_{60}$ region within the $C_{60}$ island is not a second $C_{60}$ layer on top of the latter, because the increase in height turns out to be just the thickness of a silver monolayer, i.e., 2 Å. Previous

studies[15,17] show that a second layer $C_{60}$ will not exhibit the characteristic bright-dim contrast as opposed to what is observed here. Often, additional bare silver layers are formed at the neighboring region. Note that such an "isolated" $C_{60}$ island as shown in Fig. 6 is mainly found on terraces wider than $\sim 150$ nm. The raised $C_{60}$ regions rarely exist in those $C_{60}$ islands aggregated at steps. Clearly, the displaced silver atoms are incorporated directly to the steps in these cases. We believe the observation of such mass flow and the double-layer $C_{60}$ island structure will not be unique to $C_{60}/$Ag(100); it will be a general phenomenon for fullerene films with adsorbate-induced reconstructions.

Since at low temperature all $C_{60}$ islands consist only of the bright $C_{60}$,[15] the mass flow of silver atoms is exclusively related to the dim $C_{60}$. The long-range mass transport implies that the interfacial reconstruction is not simply a mass-conserved local rearrangement of silver atoms. Instead, we apply mass conservation to those "isolated" islands to estimate the number of Ag atoms, $N$, displaced by each dim $C_{60}$. Let $S_1$, $S_2$, and $S_{Ag}$ denote the areas for the $C_{60}$ region with original height, the "higher" $C_{60}$ region, and the extra bare silver region, respectively, and $\theta_{dim}$ be the average concentration of dim $C_{60}$ in $S_1$ and $S_2$. Then

$$N \approx \frac{10.4(S_2 + S_{Ag})}{\theta_{dim}(S_1 + S_2)}, \qquad (1)$$

where 10.4 is the approximate number of silver atoms per $C_{60}$ in the (111) phase. By calculating $N$ from 15 isolated islands, which are at least $\sim 50$ nm away from any step and have sizes $(S_1 + S_2)$ ranging from $\sim 2000$ nm$^2$ to $\sim 16\,000$ nm,$^2$ we find an average $\langle N \rangle = 4.3 \pm 0.5$, where $N$ has been weighted by the total area of $S_1$ and $S_2$.

Since dim and bright $C_{60}$ can appear as nearest neighbors, the interfacial restructuring accompanied with the dim $C_{60}$ should be local. A plausible structural model to account for $N \sim 5$ involves a double-layer square pyramidal pit with $\langle 111 \rangle$ microfacets. In such a pit, four Ag atoms are removed from the first layer and one from the second layer, exposing four $\langle 111 \rangle$ microfacets. The center of the pit corresponds to the fourfold hollow adsorption site. A schematic model is shown in the inset of Fig. 6. In addition to being consistent with the experimental measurements, the proposed structure is physically sensible. For example, it requires a plausible hollow adsorption site and has low-energy $\langle 111 \rangle$ microfacets. Such a structure can serve as a starting point for further theoretical structural calculations. We also note a dim $C_{60}$ residing in such a microfaceted pit can account for a $\sim 1.3$ Å corrugation if a hard sphere $C_{60}$ diameter of 10 Å is assumed. This compares reasonably with the $\sim 1-2$ Å bright-dim height variation observed in the experiments.

The measured average $\langle N \rangle$ is smaller than the $N = 5$ of the proposed pit structure. This difference is ascribed to the medium $C_{60}$ species (**M** in Fig. 1 lower left inset) which we interpret as a $C_{60}$ residing in a single Ag vacancy ($N = 1$). Because a $N = 1$ vacancy necessitates less mass transport than that of a $N = 5$ pit, films grown at lower temperatures should have more "medium"-type $C_{60}$. This is indeed what we observe. As shown in Fig. 7, $C_{60}$ films grown at $\sim 300$ K
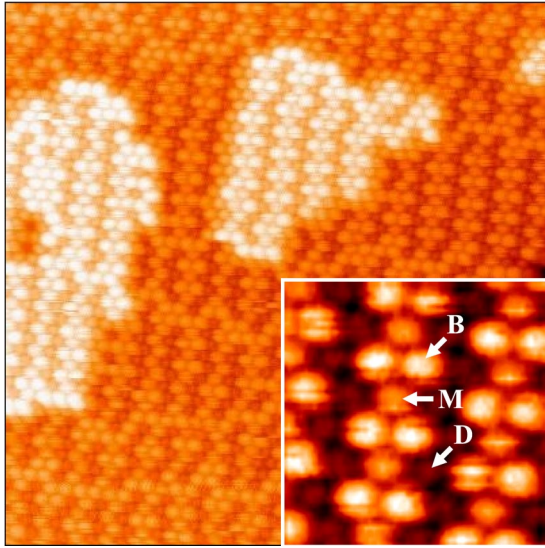
FIG. 7. (Color online) One example of the metastable structures observed in $C_{60}$ films grown at $\sim 300$ K. Here the concentration ratio of the three different $C_{60}$ contrasts is close to **B**:**M**:**D** $=2:1:2$; i.e., the concentration of **M** $C_{60}$ is $\approx 20\%$.

show various metastable structures with significantly larger concentrations of the medium $C_{60}$ species. Furthermore, as we will show in Sec. III E, the fluctuation rate between the medium and bright $C_{60}$ is the fastest. This is conceivable as a structural change between $N=0$ and $N=1$ is clearly the easiest. Both facts support our structural model.

### D. Structures and local ordering of $C_{60}$ contrast patterns

While the $C_{60}$ themselves take up the (111) close-packed structure, their bright-dim contrast does not appear to show any long-range order. Instead, the film exhibits merely short-range contrast order in several recognizable basic patterns as shown in Fig. 8: namely, (a) the zigzag structure in the $[1\bar{1}0]$ direction **A**, (b) the rectangle structure (**B**), (c) the honeycomb structure (**C**), and (d) the much less frequent line structure (**D**). The concentrations of the dim $C_{60}$ in respective idealized structures are $\theta_{dim}=1/2, 3/4, 2/3$, and $1/2$. In general, a properly annealed film ($>420$ K) contains all four
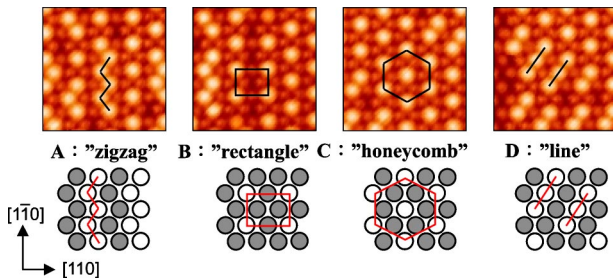


FIG. 8. (Color online) Four basic contrast patterns of the short-range contrast order in the $C_{60}/Ag(100)$ films: (a) the zigzag structure in the $[1\bar{1}0]$ direction, (b) the rectangle structure, (c) the honeycomb structure, and (d) the less frequent line structure. The concentrations of the dim $C_{60}$ ($\theta_{dim}$) in these idealized structures are $\theta_{dim}=1/2, 3/4, 2/3$, and $1/2$ for (a), (b), (c), and (d), respectively.
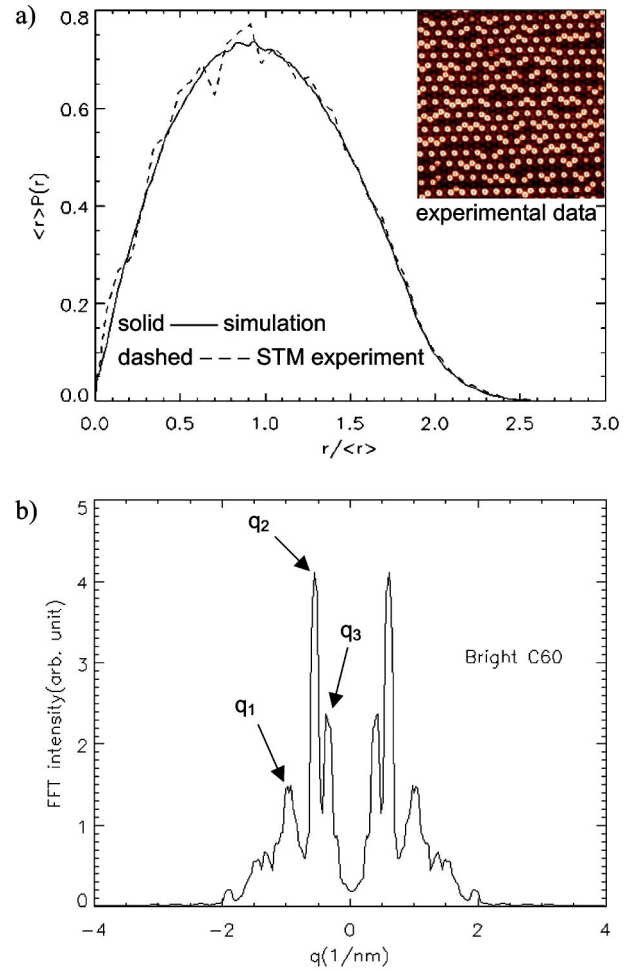


FIG. 9. (Color online) Pair correlation $P(r)$ of the bright $C_{60}$ in a typical $27\times 27$ nm$^2$ STM micrograph containing $\sim 850$ molecules is calculated. (a) The experimentally observed histogram (dashed curve) is plotted with the simulated histogram of a random distribution (solid curve) of the bright $C_{60}$. (b) The fast Fourier transform (FFT) spectrum of the difference $\Delta P(r)$ between the experiment and simulation curves indicates short-range order at $r=1/q$ $=10.2$ Å, $17.2$ Å, and $24.7$ Å. Similar results were obtained for the distribution of the rhombic tetramers (not shown).

coexisting basic patterns, yet it maintains the equilibrium concentration $\theta_{dim}\approx 2/3$. Two issues will now be addressed. First, we demonstrate that the film indeed contains only short-range order from evaluating the pair correlation function. Second, we discuss the physical origin of the four basic contrast patterns.

The pair correlation $P(r)$ of the bright $C_{60}$ in a typical $27\times 27$ nm$^2$ STM micrograph containing $\sim 850$ molecules is calculated. $P(r)$ is defined as the probability of finding two molecules at a distance $r$ in a square region.[24] In Fig. 9(a), the experimentally observed histogram is plotted together with the simulated histogram for bright $C_{60}$ randomly distributed on a (111) lattice with an identical bright $C_{60}$ concentration $\approx 0.33$. The simulated curve has been corrected for the finite-size effect of a square image.[24] The match between the two histograms, in particular at larger $r$, proves the absence of long-range correlation among the bright $C_{60}$ posi-

tions, i.e., no long-range order in the contrast pattern. At smaller distances, however, there are deviations indicating some short-range order. This is best demonstrated by the fast Fourier transform (FFT) spectrum, as shown in Fig. 9(b), of the difference $\Delta P(r)$ between the experiment and the simulation curves. The FFT spectrum shows three major peaks at $r = 1/q = 10.2$ Å, 17.2 Å, and 24.7 Å. These values correspond to the NN $C_{60}$-$C_{60}$ distance (10.0 Å), the NNN $C_{60}$-$C_{60}$ distance (17.34 Å), and the diagonal distance of a rectangle pattern unit cell (26.4 Å). Similar results were obtained for the distribution of the rhombic tetramers.

The structure and ordering of an incommensurate film with adsorbate-induced reconstruction is clearly a complicated issue. Here, we can explain the four basic contrast patterns by considering two factors: (1) $C_{60}$-induced reconstruction (i.e., "pit") occurs preferentially when $C_{60}$ occupy the most preferred registry and (2) dispacements of the incommensurate $C_{60}$ positions towards preferred binding sites. For the former, in accordance with the "pit" structural model, the bonding site for a $C_{60}$ occupying the pit will be the fourfold hollow site. For the latter, we envisage that the preferred bonding sites should be the sites with higher symmetry, i.e., hollow, bridge, and atop sites. Clearly, both processes described above can gain free energy through better coordination but they are counteracted by an energy penalty from the $C_{60}$ lattice distortion. A quantitative analysis of stable structures from these competing interactions can in principle be analyzed with the Frenkel-Kontorova model. Lacking detailed information on the microscopic energy parameters, we limit ourselves to a qualitative discussion, as follows. Consider the schematic model shown in Fig. 5(a) with the NN $C_{60}$ spacing along [110] taken as $3.5a_{Ag}$; we now ask how this structure may distort itself through the above two processes to gain energy. Note that $C_{60}$ in the type-A rows occupy alternate hollow and bridge sites. In contrast, $C_{60}$ in the type-B rows occupy non-high-symmetry sites midway between the hollow and bridge sites. The adsorption sites for these type-B row $C_{60}$ are not favorable.

For simplicity, we treat each individual type-B row as an 1D monoatomic chain. The lattice vibration modes of this 1D chain, if properly coinciding with the hollow sites, will preferentially induce the substrate reconstruction (i.e., become "dim" $C_{60}$) and the phonon modes will be "locked." Within this physical picture, we find the rectangle pattern can be regarded as an acoustic phonon with a wave vector $|k| = \pi/\langle d \rangle$, where $\langle d \rangle$ is the NN $C_{60}$-$C_{60}$ distance. The line and zigzag patterns are both acoustic phonon modes with $k = 0$. The difference between the zigzag and line patterns is that the former, on average, has zero displacement along [110] whereas the latter does not. The line pattern is therefore under a shear stress along [110] and is energetically unfavorable. Indeed, we have found very few line patterns in our experiments. If they were found, they only extend a short distance (three or four rows), unlike the zigzag pattern that can extend much farther. Why are these two phonons at the zone center and zone boundary involved? For the acoustic mode at $k = 0$, energy $\omega = 0$. It is easy to excite this mode. For the acoustic mode at $|k| = \pi/\langle d \rangle$, $\omega \neq 0$, but the group velocity $v_g = d\omega/dk = 0$. Therefore, it is a standing wave. These account for their involvement.

The idealized line, zigzag, and rectangle patterns will all have an average $3.5a_{Ag}$ NN $C_{60}$-$C_{60}$ separation along [110]. This is slightly larger than the expected average NN distance $3.46a_{Ag}$ of the $C_{60}$ film. Experimentally, the above three patterns mix and interpenetrate. It is possible that the $C_{60}$ adlayer is under local uniaxial tensile strain, depending on details of the pattern mixing. The origin of the honeycomb pattern is to compensate this excessive uniaxial tensile strain along [110]. We have measured the NN distance in the honeycomb pattern along [110]. It is about 9.7 Å and is therefore compressed from $\langle d \rangle = 10.0$ Å by 3%. In Figs. 5(b)–5(e), we illustrate the schematics of the lattice displacements of all four basic contrast patterns.

### E. Fluctuations of the bright-dim $C_{60}$ contrast

The "bright," "medium," and "dim" contrasts are not static as previously claimed in Ref. 17. They fluctuate down to ∼270 K, where the bright-to-dim $C_{60}$ transformation also starts to occur.[15] An important question is to understand whether these fluctuations are equilibrium thermal fluctuations. Furthermore, is there temporal or spatial correlation? Finally, one wishes to know the microscopic mechanisms underlying the fluctuations. Our studies provide answers to the first two questions. The last remains elusive though we can surmise some tendencies in the mass transport.

The statistics of the $C_{60}$ contrast fluctuations have been analyzed in detail. We find (1) at room temperature and above, the fluctuations are equilibrium thermal fluctuations satisfying detailed microscopic balance, (2) fluctuation probabilities show the medium and bright $C_{60}$ are quite "similar," and (3) fluctuations are uncorrelated in time and satisfy the Poisson statistics, but they are often spatially correlated. Figures 10(a) and 10(b) show two room-temperature STM images taken at the same area and 90 s apart. Figure 10(c), a composite image in which the height in Fig. 10(b) is subtracted from that in Fig. 10(a), allows us to identify unambiguously various fluctuation events. For example, in Fig. 10(c) the arrow **A** signifies a fluctuation event of a bright $C_{60}$ in (a) switching to a dim $C_{60}$ in (b) and the arrow **B** points to a fluctuation event of a medium $C_{60}$ switching to bright. Statistics over 64 images (total time 92 min) placed the concentrations of the **B**, **D**, and **M** species at 31.9%, 66.5%, and 1.6%, respectively. The fluctuation rates among them are tabulated in Table I. From the "total event counts" in Table I, it is clear that microscopic detailed balance is satisfied within statistical errors. This immediately establishes that the prepared film is indeed in a state of thermal equilibrium. It also shows that the bright and medium $C_{60}$ are similar to each other, whereas the bright-dim or medium-dim $C_{60}$ are not. The fluctuation probability for the medium to dim $C_{60}$ event (1.63%) is much smaller than that for the medium to bright $C_{60}$ event (63.2%) and is similar to that of the bright to dim $C_{60}$ event (1.61%). As we have discussed earlier, this can be understood in light of a single vacancy formation ($N = 1$) being more frequent and easier than the formation of a square pyramidal pit ($N = 5$).
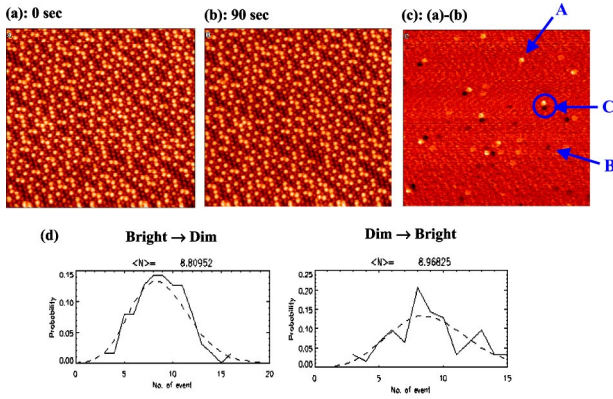
FIG. 10. (Color online) (a), (b) Two room-temperature STM images taken at 0 and 90 s of the same area. (c) A composite image by subtracting the height of (b) from that of (a). The arrow **A** points to a fluctuation event of a bright C$_{60}$ in (a) switching to a dim C$_{60}$ in (b), and the arrow **B** points to a fluctuation event of a medium C$_{60}$ in (a) switching to a bright C$_{60}$ in (b). The circle **C** shows a paired event of bright-to-dim and dim-to-bright contrast exchange. (d) Histograms of each type of fluctuation events in unit time (e.g., between consecutive STM images) satisfy the Poisson distribution.

One can investigate whether there is a temporal correlation between the fluctuation events. In Fig. 10(d), histograms of the number of fluctuation events in consecutive STM images are plotted. It shows that the switchings between the **D** and **B** (as well as others, not shown) satisfy the Poisson distribution. There is no temporal correlation and the switching probability scales linearly with the time lapse between two observations. On the contrary, there is a strong spatial correlation. Specifically, **B**→**D** and **D**→**B** events often occur in the vicinity, and so do **M**→**D** and vice versa [e.g., circle **C** in Fig. 10(c)]. For other types of switching events, e.g., **M**↔**B**, no such spatial correlation exists. This may shed some light on the microscopic origin of the mass transport involved in these fluctuations. For a **B** C$_{60}$ to become a **D** C$_{60}$, five Ag atoms have to be displaced to form a pit. This is clearly an energetically costly and kinetically slow process if all Ag atoms are moved far away. It is much more likely to occur where there are nearby Ag atom "sinks," i.e., **D** C$_{60}$ with the reconstructed pits. For fluctuations between the bright and medium C$_{60}$, no such spatial correlation exists because only one Ag atom is involved in the mass transport.

The fluctuations display strong temperature dependence as expected. They have been observed from 280 K, when the **B**-**D** contrast starts to appear, up to 400 K, when they occur so fast that tracing individual events becomes difficult. The four basic bright-dim patterns persist, however.

TABLE I. Statistics for the contrast fluctuation rates between the **B**-, **D**-, and **M**-type C$_{60}$.

| Switching event | D→M | M→D | D→B | B→D | M→B | B→M |
|---|---|---|---|---|---|---|
| Total event counts | 23 | 28 | 555 | 565 | 1081 | 1030 |
| Probability (%) | 0.031 | 1.63 | 0.76 | 1.61 | 63.2 | 2.95 |

## F. Understanding the peculiar C$_{60}$ contrast ordering: A lattice gas model

While in Sec. III D we have discussed the physical origin of the four basic contrast patterns, it remains unclear how these patterns intertwine, leading to the observed contrast pattern. It is this intricate pattern that causes the controversy on the origin of the bright-dim contrast. Here we employ a lattice gas described with a minimum set of energy parameters to model the physical interactions in this very complicated system. A C$_{60}$ film prepared at low temperature and consisting solely of the bright C$_{60}$ is taken as the zero-energy reference state. Upon annealing, some bright C$_{60}$ sites change to "dim C$_{60}$-Ag pit" sites (called simply "C$_{60}$ pit" thereafter). Second, the rhombic tetramers stabilizing specific contrast order form. Three new competing interactions now come into existence. They are the pairwise NN interactions between the C$_{60}$ pits ($E_1$ and $E_2$, $E_1$ denotes the NN interaction along [110] and $E_2$ for that in the directions 60° off [110]), the formation energy of the C$_{60}$ pit ($E_d$), and the configuration energy of the tetramers ($E_c$). The lattice gas Hamiltonian can then be expressed as

$$H = E_{ij} \sum_{i,j} n_i n_j + E_d \sum_i n_i + \sum_{conf} E_c , \qquad (2)$$

where $E_{ij}$ is $E_1$ or $E_2$, $n_i = 0$ for the bright C$_{60}$, and $n_i = 1$ for the dim C$_{60}$. We are neglecting variations in the C$_{60}$-C$_{60}$ interactions due to vertical C$_{60}$ displacements, as well as possible changes in $E_1$ due to a nonuniform separation between the C$_{60}$ pits along [110].

Several aspects of the model should be noted here. Generally, the energy for adsobate-induced surface reconstruction is separated into the energy of reconstructing the pristine surface and the difference of chemisorption energy on the reconstructed and unreconstructed surfaces. However, this approach is inconvenient because the state of substrate reconstruction is not known *a priori*. It is tempting to group the reconstruction energy by local on-site terms (i.e., formation energy) and by pairwise cross-site terms (i.e., NN interactions, etc.) in the framework of a lattice gas model. The success of this approach would have ramifications for similar models in describing ordering and phase transitions in surface films with adsorbate-induced reconstructions. Second, we note that in our model an occupied site refers to a C$_{60}$-pit complex rather than simply a C$_{60}$ molecule. For $E_1$ and $E_2$, the pairwise NN terms actually describe effective interactions between the C$_{60}$-pit complexes encompassing intermolecular, molecule-substrate, *and* substrate-substrate (i.e., pit-pit) interactions. It is unusual to employ a lattice gas species of this complexity. Finally, the tetramer configuration energy is the key ingredient in our model. This configuration energy demands a specific contrast order permutation and therefore goes beyond a direct four-body interaction. As we shall see, the key to understand the complicated ordering is the distribution of these rhombic tetramers. It allows coexistence of several structures with short-range order but its aperiodic distribution destroys long-range order. We will discuss the physical origin of the configuration energy gain before closing this section.
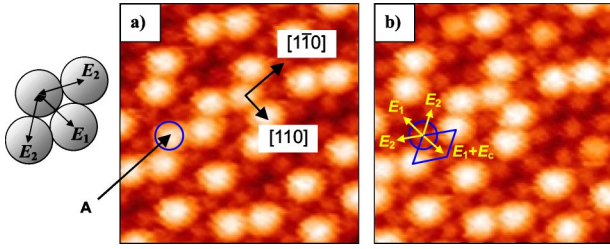
FIG. 11. (Color online) The prevalent equilibrium thermal fluctuation events of a single $C_{60}$ contrast reversal involve an energy change of $\Delta H = (2E_1 + 2E_2 + E_c + E_d)$. In (a), the interaction energy involving the **A** site is zero. The interaction energy becomes $2E_1 + 2E_2 + E_c + E_d$ in (b).
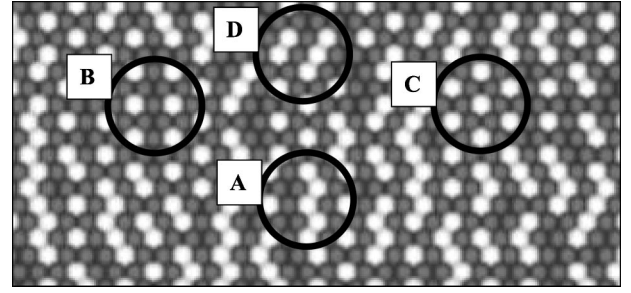


FIG. 12. A MC simulation snapshot of a $C_{60}$ lattice at the $10^4$th MC step. All the local contrast patterns (circles **A**–**D**), the equilibrium dim $C_{60}$ concentration $\theta_{\mathrm{dim}} \sim 0.65$, and the number concentration of the tetramer configuration $\sim (17 \pm 2)\%$ are successfully reproduced.

Several constraints for the parameters $E_1$, $E_2$, $E_d$, and $E_c$ can be established from the experimental data and are described here separately. (i) As shown in Fig. 8(a), the $C_{60}$ film exhibits a combination of mostly rectangle, honeycomb, and zigzag patterns with different degrees of mixing. The line pattern, less frequently observed, may be neglected here. It is easy to show that the energies per unit area for the idealized honeycomb pattern ($E_{\mathrm{honeycomb}}, \theta_{\mathrm{dim}} = 2/3$), the rectangle pattern ($E_{\mathrm{rectangle}}, \theta_{\mathrm{dim}} = 3/4$), and the zigzag pattern ($E_{\mathrm{zigzag}}, \theta_{\mathrm{dim}} = 1/2$) are $(1/3E_c + 1/3E_1 + 2/3E_2)$, $(1/4E_c + 1/2E_1 + E_2)$, and $(1/2E_2)$ respectively. The reasonable assumption that $E_{\mathrm{honeycom}} = (2/3E_{\mathrm{rectangle}} + 1/3E_{\mathrm{zigzag}})$, with $\theta_{\mathrm{dim}}$ constant, leads to $E_2 = E_c$. More accurately, since the honeycomb pattern appears more frequently after annealing, $E_c$ should be slightly more negative than $E_2$. (ii) $E_c$ and $E_d$ are negative. (iii) Fluctuations of the $C_{60}$ contrast lead to changes of local $C_{60}$ contrast configurations, and the energy changes in such events can be written in terms of the proposed Hamiltonian. Figure 11 shows an example. We focus on the fluctuation of a single $C_{60}$ at **A** changing from bright to dim. In Fig. 11(a), the interaction energy involving **A** site is zero because the molecule is a bright $C_{60}$. In Fig. 11(b), the interaction energy now becomes $E_c + 2E_1 + 2E_2 + E_d$. Since we have demonstrated equilibrium thermal fluctuations at room temperature, the enthalpy change of the above fluctuation event ($\Delta H$) satisfies $\Delta H \sim \pm k_B T$, where $k_B$ is the Boltzmann constant. In experiments, the prevalent energy change is $E_c + 2E_1 + 2E_2 + E_d$, with only a few having an energy change of $2E_1 + 3E_2 + E_d$. Interestingly, in terms of these energy changes in fluctuations, there appears no difference between the bright- and medium-type $C_{60}$. This is consistent with our previous discussion on the contrast fluctuation rates and justifies our using only the bright and dim species in the lattice gas model. To recapitulate, $\Delta H = (2E_1 + 2E_2 + E_c + E_d) \sim \pm k_B T$. (iv) A range of $E_1$ can be obtained by considering adding the dim $C_{60}$ to the idealized zigzag structure. It is easily shown that incorporation of each dim $C_{60}$ will cause an energy change of $(2E_1 + 2E_2 + E_d)$, $(2E_1 + 3E_2 - E_c + E_d)$, $(2E_1 + 3E_2 + E_d)$, $(2E_1 + 4E_2 - E_c + E_d)$, $(2E_1 + 4E_2 - 2E_c + E_d)$, or $(2E_1 + 4E_2 + E_d)$. Since $E_2 \approx E_c$ and $E_c < 0$, this energy change is at least $(2E_1 + 2E_2 + E_d)$ and at most $(2E_1 + 4E_2 + E_d)$. If $(2E_1 + 2E_2 + E_d)$ is always less than zero, then the system equilibrates at $\theta_{\mathrm{dim}} = 1$. If $(2E_1 + 4E_2 + E_d)$ is always greater than zero, then the system equilibrates at $\theta_{\mathrm{dim}} = 1/2$. Since the observed $\theta_{\mathrm{dim}}$ is

$\sim 2/3$, a necessary condition for the range of $E_1$ is $(-E_2 - 1/2E_d) < E_1 < (-2E_2 - 1/2E_d)$. Therefore, four constraints are established: (a) $E_2 \sim E_c$, with $E_c$ slightly more negative; (b) $E_c < 0$, $E_d < 0$; (c) $(2E_1 + 2E_2 + E_c + E_d) \sim \pm k_B T$; (d) $(-E_2 - 1/2E_d) < E_1 < (-2E_2 - 1/2E_d)$.

A periodic boundary condition and the traditional Metropolis algorithm were adopted in our Monte Carlo (MC) simulation. The system was thermalized by flipping the contrast of a randomly selected $C_{60}$ or switching the contrast of a NN bright-dim $C_{60}$ pair. For a $36 \times 54$ lattice, $\sim 5000$ successful steps sufficed for the attainment of equilibrium from an initial condition of $\theta_{\mathrm{dim}} = 0$ or other initial configurations. With the above four constraints, parameters could not be varied at will. To match the equilibrium concentration $\theta_{\mathrm{dim}} \sim 2/3$, trials and errors led to $E_1 = 1.5$, $E_2 = -1$, $E_c = -1.1$, $E_d = 0$, and $k_B T = 0.025$ ($T \approx 295$ K, $k_B T \approx 25$ meV). Figure 12 shows a snapshot of a $C_{60}$ lattice at the $10^4$th MC step using the above parameters. We were able to reproduce all local contrast patterns and the concentration of the tetramer configuration $\approx (17 \pm 2)\%$. Furthermore, we calculated the pair-correlation function $P(r)$ from the MC snapshot image. An analysis identical to that of Fig. 9 was conducted and Fig. 13 gives the results. The FFT spectrum shows the three preferred $C_{60}$-$C_{60}$ distances at $r = 1/q = 10.0$ Å, 17.7 Å, and 24.7 Å, consistent with the experimental findings (Fig. 9). However, the relative intensity of the FFT spectrum from the MC snapshot indicates that $P(r)$ at $\sim 10.0$ Å is overestimated and $P(r)$ at $\sim 24.7$ Å is underestimated. In the MC simulation, the occurrence of the zigzag feature is more frequent whereas the occurrence of the rectangle pattern is less frequent. Nonetheless, the basic features of the pair correlation function are well reproduced.

Note that the parameter $E_d = 0$ used in Fig. 12 is set for simplicity. From the conditions (c) and (d), a parameter set $(E_1, E_2, E_c, E_d, k_B T) = (1.5 + \mu, -1, -1.1, -2\mu, 0.025)$, with $\mu > 0$, will reproduce similar simulation results. An increase in $E_1$ introduces stronger repulsion between some NN dim $C_{60}$ pairs, and a constant equilibrium concentration $\theta_{\mathrm{dim}}$ is maintained as $E_d$ becomes more negative. Further simulations also demonstrate that the chosen $E_1, E_2, E_c, E_d$ are quite unique as they can only vary by $\sim k_B T$ to keep acceptable results.

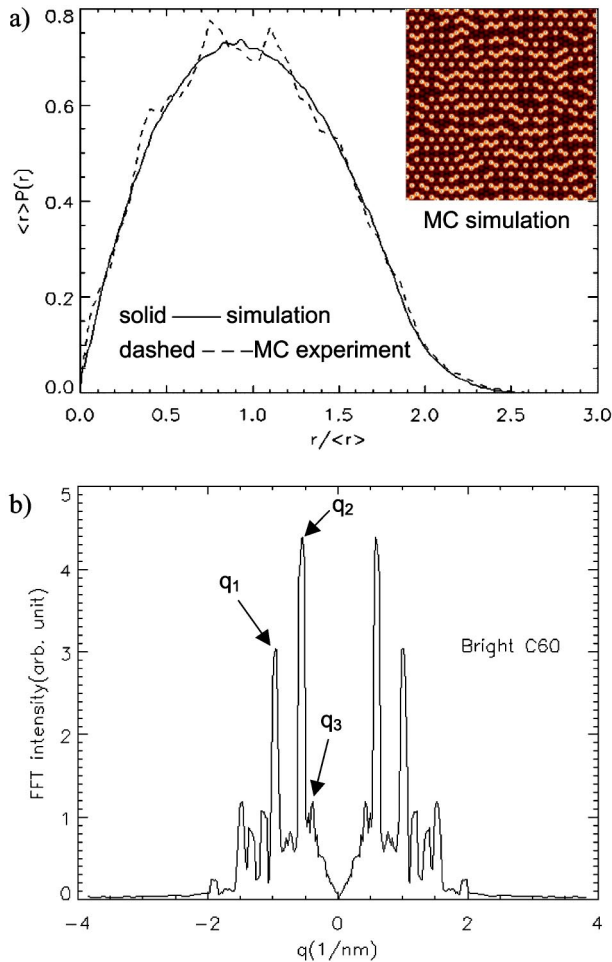If the Hamiltonian does not contain the tetramer configu-

FIG. 13. (Color online) (a) The pair correlation function $P(r)$ calculated from the MC snapshot image. (b) The FFT spectrum of $\Delta P(r)$ between the MC experiment and simulation curves shows the three preferred $C_{60}$-$C_{60}$ distances at 10.0 Å, 17.7 Å, and 24.7 Å, consistent with the experimental findings shown in Fig. 9.

ration energy term $E_c$, the simulations cannot reproduce our experimental findings with the above said parameter constraints. Often, extended line patterns are seen, as opposed to our observation, or the tetramer configuration concentration becomes significantly lower (e.g., by 50%). Thus, the distribution of the rhombic tetramers is indeed the key to understanding the complicated contrast ordering. It results in short-range order but its aperiodicity destroys long-range order. While a full account of the stability of the tetramer configuration requires full-scale first-principle calculations, some heuristic arguments are provided below. First, we note that the separation of the microfaceted pits underneath two NN dim $C_{60}$ must be integer multiples of $a_{Ag}$, e.g., $3a_{Ag}$ or $4a_{Ag}$, whereas the average $C_{60}$-$C_{60}$ distance along [110] is $3.46a_{Ag}$. In a tetramer, the separation between the pits underneath the two dim $C_{60}$ is the shorter one, i.e., $3a_{Ag}$, and a gain of interaction energy between the pits is possible.[25] There can be no such energy gain in a commensurate phase. Second, with the help of Fig. 5(a) and in view of the $3a_{Ag}$ pit separation between the dim $C_{60}$ in a tetramer, we see that the other two bright $C_{60}$ would have to sit at midway (bridge) positions ($3/2a_{Ag}$) along [110]. Presumably, this bridge ad-

sorption site is less favorable for the $C_{60}$-induced substrate reconstruction and it explains the specific contrast order in a tetramer. We also note that only the paired dim $C_{60}$ (Fig. 1, lower right inset) exhibit an intramolecular unidirectional nodal feature. These dim $C_{60}$ are thus not rotating and the van der Waals interactions between the two paired $C_{60}$ depend on their orientations. If one sums over the C-C interactions (without considering any substrate effect) for all possible unidirectional orientations for such a $C_{60}$ pair,[26] a variation in the van der Waals (vdW) energy of $\sim 150$ meV per pair at $d_1 = 9.5$ Å is possible. However, as shown in Fig. 14(a), the most favorable orientation is not reproduced experimentally. Optimal vdW interactions generally require the two neighboring $C_{60}$ to have adjacent hexagon or pentagon faces, especially at small $C_{60}$-$C_{60}$ separations. The experimentally observed orientation, as depicted in Fig. 14(b), indicates that the two $C_{60}$ face each other with opposite 6-6 bonds[18] (a 6-6 bond is the bond between two neighboring
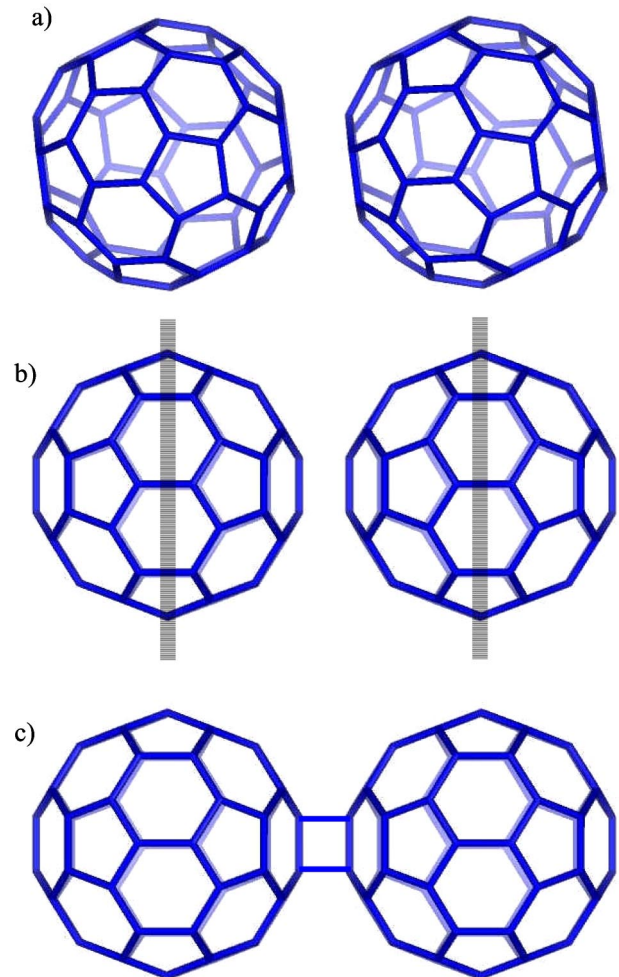


FIG. 14. (Color online) (a) The top-view structure of a $C_{60}$ pair deduced from optimizing the vdW interaction at a $C_{60}$-$C_{60}$ distance of 9.5 Å. (b) The top-view schematics of the observed orientation for the paired $C_{60}$. Nodal lines are indicated. (c) The top-view schematics of a 66/66 $C_{60}$ dimer with the [2+2] cycloadditional four-member ring oriented parallel to the substrate plane. Similarity between (b) and (c) is noted.

hexagons). It is tempting to suggest that the paired $C_{60}$ is a 66/66 $C_{60}$ dimer with the $[2+2]$ cycloadditional four-member ring[27] oriented parallel to the surface plane. This is supported by the 9.3 Å separation and the matching nodal feature of a properly oriented 66/66 dimer[18,27] illustrated in Fig. 14(c). The driving force for the formation of such dimers can be related to the short pit-pit distance ($3a_{Ag} \approx 8.67$ Å) underneath that exerts a strong compressive stress on the $C_{60}$ pair, leading to a pressured-induced $C_{60}$ dimerization.[28] This dimer dissociates when the pit- pit distance underneath increases, e.g., to $4a_{Ag} \approx 11.56$ Å, and pulls the dimer apart. The energy gain from the vdW paired $C_{60}$ to a 66/66 dimer is about 0.45 eV per $[2+2]$ cycloadduct.[27,28] This is not far from the $E_c \approx 1$ eV used in the lattice gas model. *Ab initio* calculations to clarify this provocative proposition are underway.

## IV. CONCLUSION

We have presented a detailed STM study to clarify the adlayer structure of monolayers $C_{60}$ grown on Ag(100). The topographic nature of the bright-dim contrast induced by local substrate restructuring underneath the dim $C_{60}$ is reaffirmed. The mass flow measurements, though indirect, allow us to infer a plausible structural model for the $C_{60}$-induced substrate reconstruction as a pyramidal "pit" with $\langle 111 \rangle$ microfacets. These findings have been corroborated by careful statistical analysis of the equilibrium thermal fluctuations of the $C_{60}$ contrasts. The adsorption structure of the adlayer is significantly revised; LEED measurements show that the $C_{60}$ monolayer on Ag(100) is an incommensurate (111) close-packed phase, rather than the commensurate $c(6 \times 4)$ phase reported earlier. This incommensurate phase is also aperiodic, due to a randomly distributed lateral distortion, i.e., a "rhombic tetramer" configuration with specific contrast order. Such tetramers are key to understanding the bright-dim $C_{60}$ contrast with merely short-range order. This is described by a lattice gas model incorporating a configuration energy term to elucidate the competing interactions in the reconstructed $C_{60}$-Ag(100) interface. Our work should pave a smooth way for further study to understand the structure-property relationship in this very unique and interesting fullerene/metal system.

*Corresponding author. Electronic address: wpai@ccms.ntu.edu.tw

[1] T. Sakurai, X. D. Wang, Q. K. Xue, Y. Hasegawa, T. Hashizume, and H. Shinohara, Prog. Surf. Sci. **51**, 263 (1996).

[2] O. Gunnarsson, Rev. Mod. Phys. **69**, 575 (1997).

[3] P. Rudolf, in *Proceedings of the 10th International Winterschool on Electronic Properties of Novel Materials*, edited by H. Kuzmany, J. Fink, M. Mehring, and S. Roth (World Scientific, Singapore, 1996), p. 263.

[4] A. J. Maxwell, P. A. Bruhwiler, D. Arvanitis, J. Hasselstrom, M. K. J. Johansson, and N. Martensson, Phys. Rev. B **57**, 7312 (1998).

[5] K. Binder and D. P. Landau, in *Advances in Chemical Physics*, edited by K. P. Lawley (Wiley, New York, 1989), Vol. 76, p. 91.

[6] J. K. Gimzewski, S. Modesti, and R. R. Schlittler, Phys. Rev. Lett. **72**, 1036 (1994).

[7] J. Weckesser, C. Cepek, R. Fasel, J. V. Barth, F. Baumberger, T. Greber, and K. Kern, J. Chem. Phys. **115**, 9001 (2001).

[8] W. L. Yang, V. Brouet, X. J. Zhou, H. J. Choi, S. G. Louie, M. L. Cohen, S. A. Kellar, P. V. Bogdanov, A. Lanzara, A. Goldoni, F. Parmigiani, Z. Hussain, and Z. X. Shen, Science **300**, 303 (2003).

[9] A. Goldoni and G. Paolucci, Surf. Sci. **437**, 353 (1999).

[10] C. Cepek, I. Vobornik, A. Goldoni, E. Magnano, G. Selvaggi, J. Kroger, G. Panaccione, G. Rossi, and M. Sancrotti, Phys. Rev. Lett. **86**, 3100 (2001).

[11] A. Goldoni, C. Cepek, E. Magnano, A. D. Laine, S. Vandre, and M. Sancrotti, Phys. Rev. B **58**, 2228 (1998).

[12] E. Giudice, E. Magnano, S. Rusponi, C. Boragno, and U. Valbusa, Surf. Sci. **405**, L561 (1998).

[13] T. R. Albrecht, P. Grutter, D. Horne, and D. Rugar, J. Appl. Phys. **69**, 668 (1991).

[14] C. Cepek, R. Fasel, M. Sancrotti, T. Greber, and J. Osterwalder, Phys. Rev. B **63**, 125406 (2001).

[15] W. W. Pai, C. L. Hsu, C. R. Chiang, Y. Chang, and K. C. Lin, Surf. Sci. **519**, L605 (2002); W. W. Pai and C. L. Hsu, Phys. Rev. B **68**, 121403(R) (2003).

[16] C. Cepek, L. Giovanelli, M. Sancrotti, G. Costantini, C. Boragno, and U. Valbusa, Surf. Sci. **454**, 766 (2000).

[17] G. Costantini, S. Rusponi, E. Giudice, C. Boragno, and U. Valbusa, Carbon **37**, 727 (1999).

[18] M. Grobis, X. Lu, and M. F. Crommie, Phys. Rev. B **66**, 161408 (2002).

[19] P. W. Murray, M. O. Pedersen, E. Laegsgaard, I. Stensgaard, and F. Besenbacher, Phys. Rev. B **55**, 9360 (1997).

[20] J. Weckesser, J. V. Barth, and K. Kern, Phys. Rev. B **64**, 161403 (2001).

[21] A. P. Smith and N. W. Ashcroft, Phys. Rev. Lett. **59**, 1365 (1987).

[22] P. A. Heiney, J. E. Fischer, A. R. McGhie, W. J. Romanow, A. M. Denenstein, J. P. McCauley, A. B. Smith, and D. E. Cox, Phys. Rev. Lett. **66**, 2911 (1991).

[23] J. Frenkel' and T. Kontorova, J. Phys. (Moscow) **1**, 137 (1939).

[24] J. Repp, F. Moresco, G. Meyer, K. H. Rieder, P. Hyldgaard, and M. Persson, Phys. Rev. Lett. **85**, 2981 (2000).

[25] R. V. Kukta, A. Peralta, and D. Kouris, Phys. Rev. Lett. **88**, 186102 (2002).

[26] L. A. Girifalco, J. Phys. Chem. **95**, 5370 (1991).

[27] J. Nakamura, T. Nakayama, S. Watanabe, and M. Aono, Phys. Rev. Lett. **87**, 048301 (2001).

[28] T. L. Makarova, Semiconductors **35**, 243 (2001).